Raman-like light scattering from acoustic phonons in photonic crystal fiber

P. Dainese[*], P. St.J. Russell[†], G. S. Wiederhecker[*], N. Joly[†], H. L. Fragnito[*], V. Laude[‡] and A. Khelif[‡]

*CePOF, Instituto de Física, Universidade Estadual de Campinas, Brazil
†Max-Planck Research Group (IOIP), University of Erlangen-Nuremberg, Germany
‡Département LPMO, Institut FEMTO-ST, Besançon, France
pdainese@ifi.unicamp.br ; russell@optik.uni-erlangen.de

Abstract: Raman and Brillouin scattering are normally quite distinct processes that take place when light is resonantly scattered by, respectively, optical and acoustic phonons. We show how few-GHz acoustic phonons acquire many of the same characteristics as optical phonons when they are tightly trapped, transversely and close to modal cut-off, inside the wavelength-scale core of an air-glass photonic crystal fiber (PCF). The result is an optical scattering effect that closely resembles Raman scattering, though at much lower frequencies. We use photoacoustic techniques to probe the effect experimentally and finite element modelling to explain the results. We also show by numerical modelling that the cladding structure supports two phononic band gaps that contribute to the confinement of sound in the core.

References and Links

1. T. A. Birks, D. Culverhouse, and P. St. J. Russell, "The acousto-optic effect in single mode fiber tapers and couplers," J. Lightwave Tech. **14**, 2519-2529 (1996)
2. M. Trigo, A. Bruchhausen, A. Fainstein, B. Jusserand, and V. Thierry-Mieg, "Confinement of acoustical vibrations in a semiconductor planar phonon cavity," Phys. Rev. Lett. **89**, 227402 (2002).
3. P. St. J. Russell, "Light in a tight space: enhancing matter-light interactions using photonic crystals," Proc. Conf. Nonlinear Optics (Optical Society of America) **79**, 377-379 (2002).
4. T. Gorishnyy, C. K. Ullal, M. Maldovan, G. Fytas and E. L. Thomas, "Hypersonic phononic crystals," Phys. Rev. Lett. **94**, 115501 (2005).
5. P. St. J. Russell, "Photonic crystal fibers," Science **299**, 358-362 (2003).
6. P. Dainese, N. Joly, E. J. H. Davies, J. C. Knight, and P. St. J. Russell, and H. L. Fragnito "Stimulated Brillouin scattering in small-core PCF," in Proceedings of Conference on Lasers & Electro-Optics CLEO'04 (2004).
7. P. St. J. Russell, E. Marin, A. Diez, and A. B. Movchan, "Sonic band gaps in PCF preforms: enhancing the interaction of sound and light," Opt. Express **11**, 2555-2560 (2003).
8. V. Laude, A. Khelif, S. Benchabane, M. Wilm, T. Sylvestre, B. Kibler, A. Mussot, J. M. Dudley and H. Maillotte, "Phononic band-gap guidance of acoustic modes in photonic crystal fibers," Phys. Rev. B **71**, 045107 (2005).
9. E. M. Dianov, A. V. Luchnikov, A. N. Pilipetskii, and A. N. Starodumov, "Electrostrictive mechanism of soliton interaction in optical fibers," Opt. Lett. **15**, 314-316 (1990).
10. L. du Mouza, Y. Jaouën, and C. Chabran, "Transverse Brillouin effect characterization in optical fibers and its geometrical aspects," IEEE Photon. Technol. Lett. **10**, 1455-1457 (1998).
11. R. M. Shelby, M. D. Levenson and P. W. Bayer, "Guided acoustic-wave Brillouin scattering," Phys. Rev. B **31** 5244–5252 (1985)
12. N. Shibata, A. Nakazono, N. Taguchi, and S. Tanaka, "Forward Brillouin scattering in holey fibers," IEEE Photon. Technol. Lett. **18**, (412-414) 2006
13. R. A. Waldron, "Some problems in the theory of guided microsonic waves," IEEE Trans. Microwave Theory & Techniques **MTT-17**, 893–904 (1969).
14. R. N. Thurston, "Elastic waves in rods and clad rods," J. Acoust. Soc. Am. **64**, 1–37 (1978).
15. D. Culverhouse, F. Farahi and P.St.J. Russell, "Experimental observation of forward SBS in dual-mode single-core fiber," Electron. Lett. **26**, 1195-1197 (1990).

16. P. St. J. Russell, D. Culverhouse, and F. Farahi, "Theory of forward stimulated Brillouin scattering in dual-mode single-core fibers," IEEE J. Quant. Electron. **27**, 836-842 (1991).
17. J. F. Nye, *Physical Properties of Crystals* (Oxford University Press, 1985).
18. M. Wilm, K. Khelif, S. Ballandras, V. Laude and B. Djafari-Rouhani, "Out-of-plane propagation of elastic waves in two-dimensional phononic band-gap materials,'" Phys. Rev. E **67**, 065602 (2003).
19. S. Guenneau and A. B. Movchan, "Analysis of elastic band structures for oblique incidence," Archive for Rational Mechanics and Analysis, **171**, 129-150 (2004).
20. A. Yariv and P. Yeh, *Optical Waves in Crystals* (John Wiley & Sons, New York, 1984).
21. C. Krischer, "Optical measurements of ultrasonic attenuation and reflection losses in fused silica," J. Acoust. Soc. Am. **48**, 1086-1092 (1970)
22. D. Elser, U. L. Andersen, A. Korn, O. Glöckl, S. Lorenz, Ch. Marquardt, and G. Leuchs, "Reduction of guided acoustic wave Brillouin scattering in photonic crystal fibers," arXiv:quant-ph/0512044 v1, 6 Dec 2005.

1. Introduction

Tight confinement of light and sound strongly alters acousto-optic interactions through the appearance of discrete acoustic bound states [1-4]. In glass-air photonic crystal fibers (PCFs [5]), the complex geometry and "hard" boundaries provide strong acoustic reflections that couple all three displacement components (radial $\hat{r}$, azimuthal $\hat{\phi}$ and axial $\hat{z}$). As a result, no mode is purely shear (S) or longitudinal (L) in character, and mixed S and L acoustic resonances appear in the core, strongly altering the Brillouin scattering characteristics. We recently reported that the backward Brillouin scattering spectrum in ultra-small-core PCF displays multiple bands arising from different types of core-guided acoustic modes [6]. Here we report on forward Brillouin scattering (FBS) in these PCFs, where the very high air-filling fraction permits sound at frequencies of a few GHz to be trapped purely in the transverse plane by phononic band gap effects [7,8]. The ability to confine acoustic energy at zero axial wavevector $\beta_{ac} = 0$ means that the ratio of frequency ω_{ac} to wavevector β_{ac} becomes arbitrarily large as $\beta_{ac} \to 0$, and thus can easily match the value for the light guided in the fiber, c/n. This permits phase-matched interactions between the acoustic mode and two spatially identical optical modes of different frequency. Under these circumstances the acoustic mode has a well-defined cut-off frequency ω_{co} above which its dispersion curve – plotted on an (ω, β) diagram – is flat (see the schematic in Fig. 1), similar to the dispersion curve for optical phonons in diatomic lattices. The result is a scattering process that is Raman-like (i.e., the participating phonons are optical-phonon-like), even though it makes use of acoustic phonons; Brillouin scattering is turned into Raman scattering, power being transferred into an optical mode of the same order, frequency-shifted from the pump frequency by the cut-off frequency.
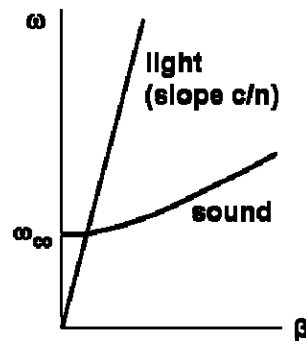

Fig. 1. Schematic dispersion relation for acoustic modes, illustrating the optical-phonon-like branch at zero acoustic wavevector and the phase-matching point at the intersection with the optical dispersion line.

A signature of acoustic resonances in standard single-mode optical fiber (SMF) [9-11] and large-core PCF [12] is the appearance of frequency side-bands in the transmitted light. This can be studied by photoacoustic excitation using short laser pulses (~50 ps) and a second

continuous-wave (CW) probe laser. In these experiments, a passing optical pulse excites many different transverse acoustic resonances at the same moment, in the case of SMF producing a pulse of acoustic energy that traverses the fiber, is reflected at the outer cladding boundary and then returns to the core, somewhat broadened by acoustic dispersion, to perturb the optical field once more. For a co-propagating continuous wave mode, the result is a sequence of pulsed changes in optical phase, the temporal spacing being equal to the round-trip time (core to cladding edge to core) in the fiber. The acoustic pulse can be viewed as containing a broad spectrum of discrete individual acoustic resonances of the fiber cross-section – which are spectrally very dense in a fiber with diameter 125 μm, i.e., their free spectral range is small. In the case of a PCF with a very small core surrounded predominantly by air, however, the core boundary acts as a strong reflector for sound, the round-trip time is very much shorter and the free spectral range of the resonances is much larger; the effect is even more pronounced if a phononic band gap exists in the cladding. As a result the acoustic response is much more sinusoidal, containing at most only a few dominant frequencies, resulting in a very "clean" quasi-Raman spectrum. Although higher frequency resonances may also be excited, these will suffer higher acoustic absorption (which scales as the square of the frequency) and will have a multiple nodes in their transverse field pattern, resulting in poor overlap with the optical core mode.

In the next two sections we explain the quasi-Raman picture in more detail, describe the experimental set-up used in the photo-acoustic measurements and present experimental results. In section 4 we make use of numerically derived solutions of the acoustic wave equation to understand the core-confined acoustic resonances and explain the photoacoustic measurements. Finally in section 5 we draw conclusions.

2. Quasi-Raman scattering

Raman and Brillouin scattering proceed when the pump light, the scattered frequency-shifted light and the associated phonon (optical for Raman & acoustic for Brillouin) satisfy the conservation relation:

$$(\beta_{pump}, \omega_{pump}) - (\beta_{scatt}, \omega_{scatt}) = \pm(\beta_{ph}, \omega_{ph}) \tag{1}$$

where the + sign refers to Stokes (frequency down-shifted) scattering and the − sign to anti-Stokes scattering. In (1) all the frequencies are positive-definite quantities, and the wavevectors are in general nonlinear functions of frequency $\beta_i = \omega n_i(\omega)/c$ where the refractive index of each wave $n_i(\omega)$ is defined as the inverse phase velocity of the wave measured in units of the inverse speed of light c^{-1}. For acoustic phonons in bulk materials, n_{ph} is typically some five orders of magnitude larger than for light, so that (1) can only be satisfied by backward light scattering ($\beta_B < 0$) at acoustic frequencies of order 10 GHz. When, however, the sound is trapped in the transverse plane within a PCF core, the situation is very different, as we now illustrate by treating the core as a perfectly confining cylindrical waveguide (this is an approximate model used to highlight the physics – a complete numerical analysis will be presented later). This yields the acoustic dispersion relation:

$$\beta_{ph} = \frac{n_{ac}}{c}\sqrt{\omega_{ph}^2 - \omega_{co}^2} \tag{2}$$

for the fundamental mode where n_{ac} is the acoustic refractive index of the bulk material as defined above (5.02×10^4 for L waves and 7.97×10^4 for S waves), $\omega_{co} = c z_{mn}/a n_{ac}$ is the cut-off frequency of the core, a being its radius, and z_{mn} is the appropriate zero of a functional relation containing Bessel functions [13,14]. For a core diameter of 1.1 μm this yields a cut-off frequency in the range 2-3 GHz. If we assume that the wavevector of the guided optical modes, in the vicinity of the pump laser frequency, takes the form $\beta = \beta_o + \omega n_o/c$ (this

allows for local dispersion), then it is straightforward to show that (1) is satisfied for a frequency shift:

$$\omega_{ac} = \frac{\omega_{co}}{\sqrt{1-(n_o/n_{ac})^2}} \simeq \omega_{co} .$$

(3)

Perhaps the most striking feature of this solution is that it is independent of pump laser frequency (as in Raman scattering), within the (very good) approximation that the optical wavevector is a linear function of frequency. This renders the scattering process quite dissimilar to normal backward Brillouin scattering, where the frequency shift scales linearly with the pump frequency $\omega_{ac} \simeq 2\omega_p n_o/n_{ac}$, or to FBS between non-degenerate optical modes with refractive indices n_1 and n_2 when $\omega_{ac} \simeq |n_1-n_2|\omega_p/n_{ac}$ [15,16].

3. Experimental methods

Since in any Raman or Raman-like scattering process the frequency shift depends only very weakly on the pump frequency, it is possible to carry out photo-acoustic pump-probe measurements of the acoustic resonances following the technique briefly introduced above [9-10,12]. The experimental setup is shown in Fig. 2.
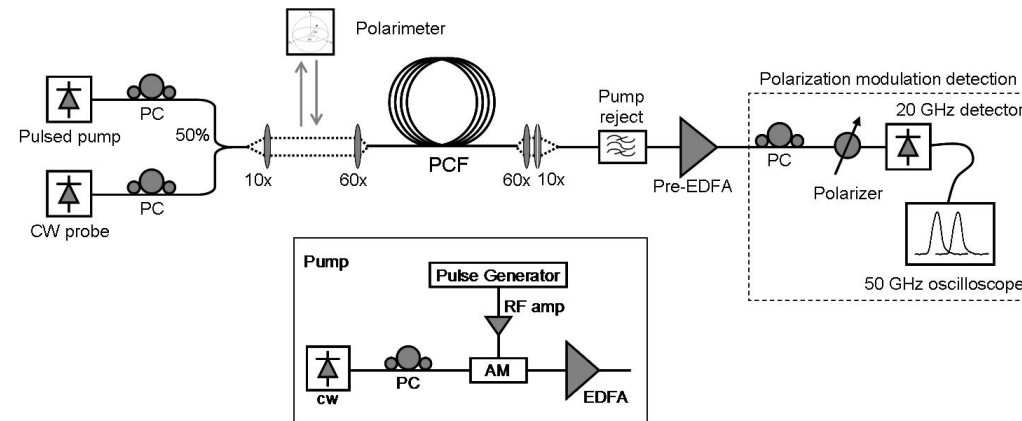

Fig. 2. Experimental setup used to perform photoacoustic pump-probe measurements. Inset: Pump modulation scheme. A CW external-cavity diode laser (~ 200 kHz linewidth) was amplitude-modulated using a lithium-niobate external modulator. A pulse generator produced 100 ps (FWHM) electrical pulses at 15 MHz repetition rate, which were then amplified using a wideband radio-frequency amplifier (26 GHz). The resulting optical pulses were then amplified in a 2W erbium doped fiber amplifier (EDFA), resulting in pulse energies of ~100 pJ. The CW probe was an external-cavity diode laser oscillating at 1530 nm (~ 200 kHz linewidth) with 10 mW of power.

A pulsed pump laser (at 1561 nm) was combined with the CW probe laser (at 1530 nm) using a 50% fiber coupler, and launched into the PCF using a pair of microscope lenses. The inset shows the pulsed pump source scheme (a detailed description is found in the caption). The input lenses were spatially separated so that we could insert a polarimeter between them to measure both pump and probe states of polarization at the fiber input (polarization controllers were used to change the input states of polarization). A second pair of lenses collected the light leaving the PCF. A band-pass optical filter (0.5 nm FWHM) rejected the pump laser light and a low-noise optical pre-amplifier was used to amplify the probe signal after the filter. A final polarization controller and a polarizer were used to convert polarization modulation (caused by the acoustic resonances) into amplitude modulation, the signal being detected by a fast photodiode (30 GHz) and analyzed using an oscilloscope (50 GHz bandwidth).

The two PCFs used in our experiments had core diameters of 1250 nm (PCF#1) and 1220 nm (PCF#2), and large air-filling fractions [Fig. 3(a)]. The cores were supported by thin glass

webs that were slightly asymmetric in thickness and length, due to fluctuations during manufacture. Both fibers displayed strong birefringence, so we also measured the orientation of the principal axes with respect to the fiber structure, as shown in Fig. 3(b); the fast axis is aligned with the vertical webs. To measure the birefringence we directly detected the pulses leaving the PCF. When the pump polarization is aligned between the principal axes, orthogonally polarised pulses are excited, each travelling at a different velocity and thus arriving at a different time. For example, PCF#2 is 84 m long and produces a 112 ps difference in arrival time between principal states, easily measurable in our system; this delay corresponds to a birefringence of 0.0004. A polarimeter was used to confirm that the pump is linearly polarized and also to orient the probe polarization with respect to the pump. The fiber was then cleaved close to the fiber holder and inspected in a 400x microscope to identify the orientation of the fast and slow axes relative to the hexagonal cladding structure. These axes are drawn on the SEM in Fig. 3(b).
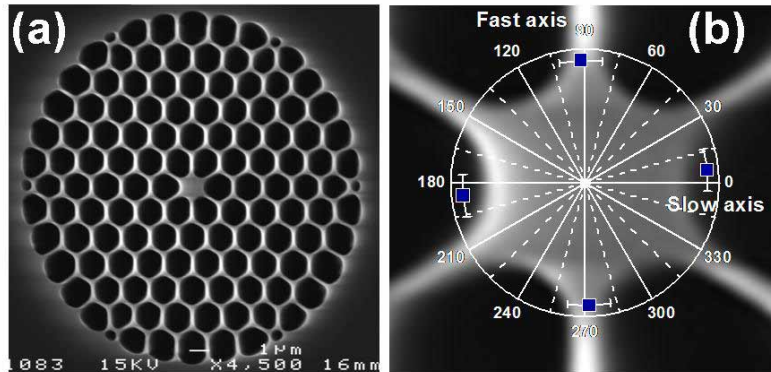

Fig. 3. (a) Scanning electron micrograph of the PCF cross-section; (b) zoomed image of the core, showing the orientation of the principal optical axes relative to the PCF structure. A polarimeter was used to characterize the polarization states of the principal axes; these were then compared with pictures of the fiber input and output faces, taken using a reflection microscope. The error bars indicate the experimental uncertainty.

We aligned the pump polarization along the slow axis, and adjusted the probe polarization so as to launch equal amounts of light along each major axis. The result for an 84 m length of PCF#2 is presented in Fig. 4 (probe left-circularly polarized), where the detected signal (in mV) is plotted against time. In contrast to standard fiber, where the impulse response is a sequence of spiked changes in phase or polarization (spaced by 21 ns and 33 ns corresponding to reflections of longitudinal and shear waves at the 125 μm outer clad surface [10]), we observed a continuously modulated signal over the entire 50 ns measurement window – a clear signature of the presence of only a few acoustic resonances confined to the core.

Assuming that the principal axes of the acoustically induced birefringence coincide with the fiber principal axes, maximum visibility for a circularly polarized probe is obtained when the polarizer is oriented at 45° with respect to the axes – the component along the fast axis (say y) serves as a local oscillator to detect the phase-modulation of the slow axis component (say x), and vice-versa. In this case the detected signal for small index perturbation is approximately given by
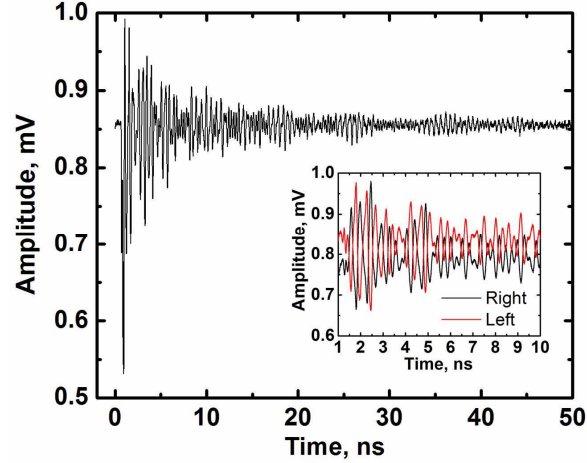
Fig. 4. Measured photoacoustic impulse response in PCF#2 (core diameter 1.22 µm). Inset: complementary signals obtained for right and left circular probe polarization.

$$V = \bar{V} \left[1 \pm \frac{2\pi L}{\lambda} \Delta n(t) \right] \tag{4}$$

where $\Delta n = \Delta n_y - \Delta n_x$ is the difference between the induced index perturbations along the fast (Δn_y) and slow (Δn_x) axis respectively, $\bar{V}$ is the DC level of the detected signal, and the signals + and − apply respectively to right and left circular polarization. The plot in the inset of Fig. 4 compares the signals when the probe is right and left circularly polarized. The almost perfect complementarity, in agreement with (4), is proof of the reliability of the experimental method (the small difference in DC level is caused by polarization-dependent loss).
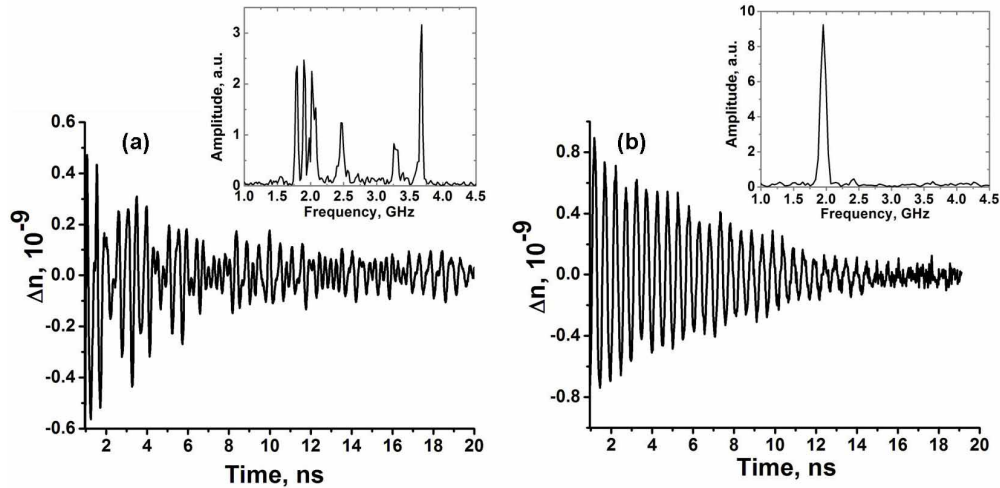

Fig. 5. Measured index modulation due to photoacoustic excitation of acoustic modes in small core PCFs. The responses were recorded for two PCFs with core radius & length (a) PCF#2: 610 nm & 84 m; (b) PCF#1: 625 nm & 87 m. Insets: Fourier transforms of the impulse responses (amplitudes).

We performed the same measurement for PCF#1 (87 m long), and the result is shown in Fig. 5, together with that obtained for PCF#2 for comparison (pump polarization along the slow axis). We used (4) to directly plot the index perturbation. We see that the impulse

response obtained for the slightly larger core (PCF#1) is a single frequency decaying oscillation, in contrast to PCF#2 where beating between several frequencies is evident. The Fourier transforms of the response for both PCFs are also shown in Fig. 5 and confirm our statement (note that the transient shock signals for $t < 1$ ns were excluded from the Fourier transforms). In PCF#1 a strong single peak at 1.97 GHz is observed while in PCF#2 several peaks are seen as expected from the temporal response.

To explore the differences in the observed spectra we carried out measurements of the spontaneous scattering due to thermally-excited acoustic modes, following the procedure reported in [11]. The result for PCF#2 is shown in Fig. 6(a) and a comparison for both fibers is shown in Fig. 6(b). We again confirm a single peak at 1.97 GHz for PCF#1 and clearly see that in PCF#2 the strongest band at 2 GHz is split into several peaks, possibly due to asymmetries in the core or its supporting webs. Although these measurements (Fig. 6) are useful as a guide to the features seen in the Fourier transform of the photoacoustic response, a quantitative comparison is not appropriate because the phonons involved in the photoacoustic interaction originate from electrostriction, while those in the spontaneous measurement are thermally excited.
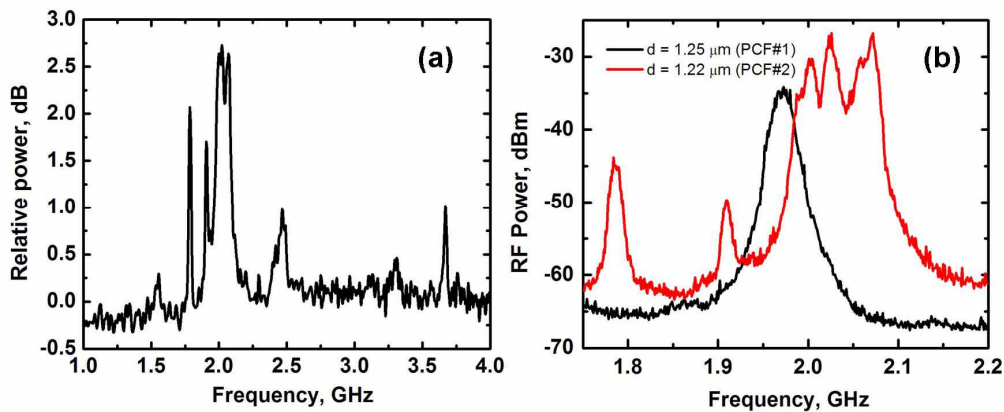

Fig. 6. (a) Spontaneous forward Brillouin scattering spectrum for PCF#2. The spectrum was obtained using a polarization spectroscopy technique [11]. The vertical scale is logarithmic and the 0 dB level corresponds to the shot-noise limit. The instrument spectral response had 1 MHz electronic resolution. (b) Comparison of the spontaneous forward Brillouin scattering spectra for PCF#1 and PCF#2. Both present a dominant peak around 2 GHz, and in PCF#2 this peak is split into 3 sub-peaks possibly due to structure asymmetries.

4. Discussion & analysis of results

The results show that pulse-driven electrostriction creates oscillating optical birefringence in the core, implying that a component of core motion must exist that makes it expand along one principal axis while expanding less (or even contracting) along the other. We attribute this partly to azimuthal and radial distortions in the core and the structure surrounding it (an acoustic resonance that would be purely radial in a core with perfect hexagonal symmetry is in fact distorted, inducing extra birefringence), and partly to anisotropic terms in the electrostriction [17]. The net result is an oscillating anisotropic strain field that modulates the birefringence. For cores with higher levels of structural distortion, such as PCF#2, the acoustic resonances will split into separate frequencies, each corresponding to a different strain field polarization, and a beat-note will appear in the measured signal, as seen in Fig. 5. The absence of a beat-note in PCF#1 suggests that this splitting is much smaller, in keeping with the more symmetric structure of the core.

To explain the observations quantitatively, we modelled numerically the acoustic modes of the core structure in PCF#2 using an approach previously reported [18, 19]. A non-uniform discretization mesh was created from a scanning electron micrograph (including two rings of holes) and the full-vectorial acoustic wave equation was solved using finite element

techniques with clamped external boundary conditions [8]. The result is a precise representation of the discrete acoustic modes and their resonant frequencies for $\beta_{ac} = 0$. Using the same numerical approach, we calculated the optical eigenmodes of the PCF, polarized along the x (slow) and y (fast) axes. For each acoustic resonance, the distribution of the refractive index perturbation was calculated using the impermeability tensor [20] and its overlap integral with the optical mode evaluated. In this way we obtained the induced changes Δn_x and Δn_y in the effective optical mode indices.
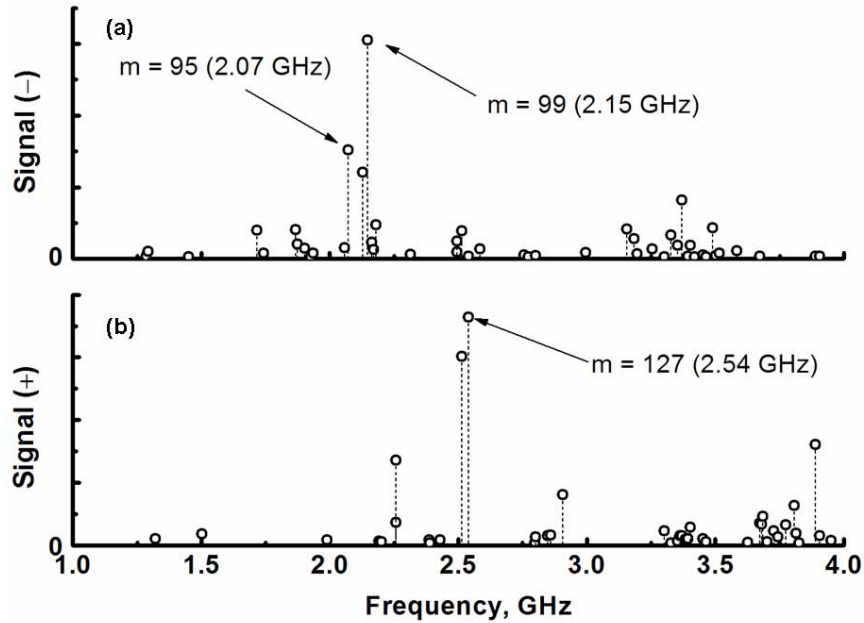

Fig. 7. Plot of the even (Signal(+)) and odd (Signal(−)) spectra for the numerically-evaluated acoustic modes of PCF#2. The vertical scale is linear (in arbitrary units) and signals weaker than 1% of the highest peak in each spectrum were removed from the plot. The strongest peaks are identified in each spectrum (*m* being the mode number) and movies for the in-plane acoustic displacements are shown in Fig. 8.

For conventional fiber, treated simply as a circular strand, analytical solutions for the transverse acoustic modes can readily be obtained and separated into families with different symmetries [11]. Those that efficiently interact with light are the radial symmetric R_{0m} modes, which cause isotropic index perturbations and do not induce birefringence, and the torsional-radial TR_{2m} modes, which induce birefringence. It is obvious that $\Delta n_{(-)} = \Delta n_y - \Delta n_x = 0$ for the R_{0m} modes, whereas $\Delta n_y = -\Delta n_x$ and $\Delta n_{(+)} = \Delta n_y + \Delta n_x = 0$ for the TR_{2m} modes (the last due to their $\cos 2\phi$ and $\sin 2\phi$ azimuthal dependence). The more complicated acoustic modes in PCF can be numerically sorted into families with different symmetries by evaluating $\Delta n_{(+)}$ and $\Delta n_{(-)}$. Predominantly R_{0m} modes will appear stronger in the $\Delta n_{(+)}$ spectrum while the predominantly TR_{2m} modes are stronger in the $\Delta n_{(-)}$ spectrum. The results are displayed in Fig. 7, where even ($\mathrm{Signal}(+) = \Delta n_{(+)}^2$) and odd ($\mathrm{Signal}(-) = \Delta n_{(-)}^2$) signals are plotted; these quantities are proportional to the sideband power created by each acoustic mode and are thus suitable for comparison with the measured spontaneous spectra. We note first that in both spectra only very few acoustic modes are able to modulate the light efficiently, as observed experimentally. The dominant peak in the even spectrum is at 2.54 GHz while in the odd spectrum there are strong peaks at 2.07 GHz and 2.15 GHz, also in good agreement with the experiments. Movies for these 3 modes are available in Fig. 8, and illustrate the radial and the torsional-radial characteristics of the dominant peaks. Another interesting characteristic of

Fig. 7 is that, since the actual PCF structure is not perfectly symmetrical, the peaks around 2.5 GHz (dominant in the even spectrum) are also present in the odd spectrum. This may explain why more modes are observed in one PCF (less symmetric) than in the other (more symmetric).
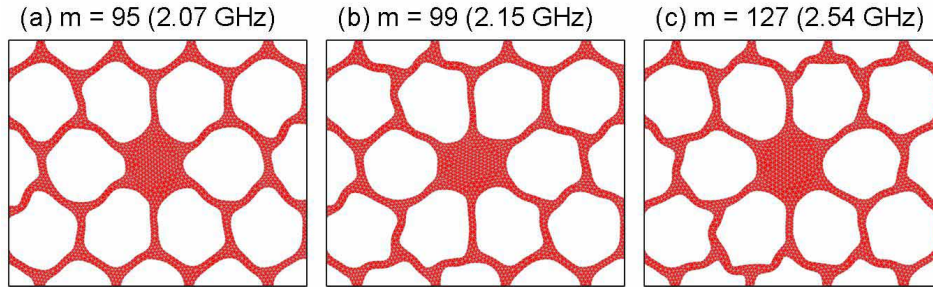
(a) m = 95 (2.07 GHz)   (b) m = 99 (2.15 GHz)   (c) m = 127 (2.54 GHz)

Fig. 8. Movies of the in-plane displacement for the acoustic modes that yield the strongest index perturbation in both Signal(+) and Signal(−), as identified in Fig. 7.

The presence of a small number of discrete resonances indicates that acoustic energy is strongly confined, suggesting that phononic band gaps must exist in the cladding at these frequencies. To test this, we numerically calculated the phononic band structure for in-plane acoustic displacements at $\beta_{ac} = 0$, using the unit cell shown in the inset in Fig. 9. Two strong band gaps appear, their positions and widths depending on the thickness of the glass webs, as explored in the "gap-map" in Fig. 10. Estimating from the scanning electron micrographs that the web thickness are ~110±15 nm (difficult to measure precisely), then from Fig. 10 we see that a structure with webs 120 nm thick has band gaps at ~1.9 GHz and ~2.5 GHz, coinciding with the frequencies measured in the photoacoustic experiments. We believe this is further evidence that phononic band gaps play an important role in the experiments. An important consequence of confining acoustic vibrations in ultra-small cores (areas of order 1 μm^2) is that thermal energy $\frac{1}{2} k_B T$ per phonon mode will produce much larger refractive index changes than in conventional fibers, yielding stronger spontaneous scattering signals than those seen in GAWBS (guided acoustic-wave Brillouin scattering) and raising the possibility of observing stimulated FBS at higher pump power levels.
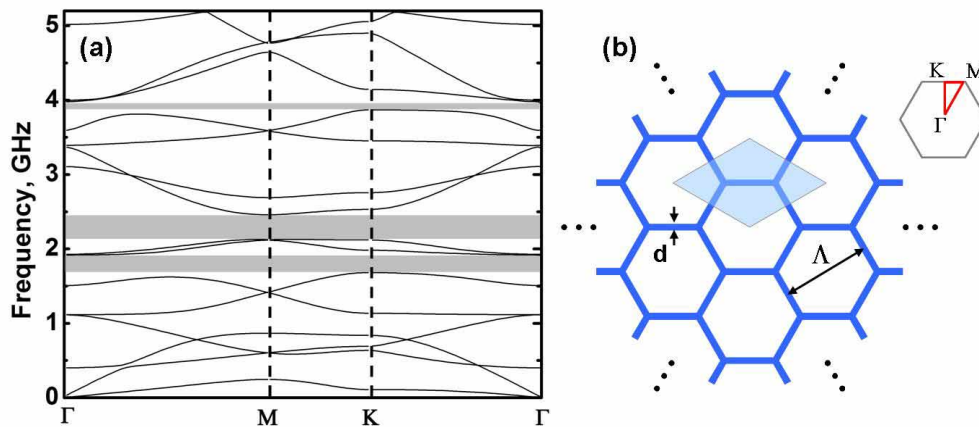

Fig. 9. (a) Phononic band structure (in-plane displacements) for a crystal formed from the unit cell highlighted in (b), with a web thickness of 110 nm. Three clear phononic band gaps are present at 1.8 GHz, 2.38 GHz and 3.93 GHz (grey). (b) Crystal structure used to calculate the phononic band structure for in-plane acoustic displacements at $\beta_{ac} = 0$.
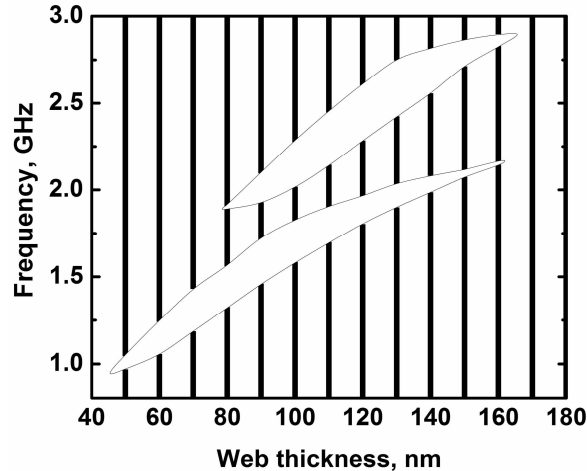
Fig. 10. The position of the phononic band gap edges as a function of web thickness for the tiled structure in Fig. 9. The vertical lines represent frequencies that can propagate in the structure. The grey line connecting the band edges is just a guide for the eye.

Finally, a comment on the lifetime of the resonances. In both PCFs this is of order 10 ns, which translates to a Q-factor of $40\pi \simeq 120$. Assuming that the acoustic energy is concentrated in the core and that only bulk acoustic losses contribute to the lifetime of the resonance, this leads to an effective acoustic absorption rate of 25 mm^{-1}, some ~20 times higher than one would expect assuming that absorption depends on the square of the acoustic frequency [21]. This suggests that the acoustic energy is not perfectly confined to the core, possibly because the phononic crystal cladding is not thick enough, so that acoustic energy can tunnel out into the solid outer cladding of the PCF. These issues require further clarification and will be addressed in future papers.

5. Conclusions

The periodic micro/nano-structuring in ultra-small core PCFs strongly alters the acoustic properties compared to conventional SMF. The periodic air-glass cladding crystal supports up to two phononic band gaps that permit strong transverse confinement of acoustic energy in the core at certain resonant frequencies. The result is an optical forward scattering process that is Raman-like in nature, even though acoustic phonons are used. The results open up fresh possibilities for manipulating sound, and may lead to new classes of ultra-efficient acousto-optic device in which both sound and light are controlled with precision and their interactions enhanced. It may also be possible to reduce unwanted noise in fiber-based nonlinear optical experiments on squeezing [22]. Used in stimulated mode, this effect may permit generation of combs of frequencies spaced by ~2 GHz at 1550 nm wavelength.